Three-dimensional modeling of a plasma in a strong azimuthal magnetic field

Luis Leal*
Lawrence Livermore National Laboratory, Livermore, California 94550, USA

Andrei Maximov, Fernando García-Rubio, and Riccardo Betti
Laboratory for Laser Energetics, University of Rochester, Rochester, New York 14623, USA

Vladimir Ivanov
University of Nevada, Reno, Reno, Nevada 89557, USA

(Received 1 May 2023; accepted 8 December 2023; published 24 January 2024)

Three-dimensional magnetohydrodynamic simulations are able to model the generation of disk-shaped plasma, driven by laser ablation from a current-carrying rod in a pulsed-power machine producing azimuthal magnetic fields of $2-3$ MG. The plasma at such extreme conditions is unique in that the parameter space for the plasma β and Hall parameter χ transition from below unity to greater than unity at different stages of the plasma generation. In simulations, the formation of the plasma disk in the azimuthal direction is driven by heat flux from the laser spot and depends on the set of transport coefficients used in simulations. The most recent set of transport coefficients leads to the formation of plasma ejecta at the back end of the rod, which qualitatively matches experiments. Specifically, the cross-gradient Nernst effect, which twists the magnetic field, is shown to have a large effect on the shape of the back-end ejecta. In the direction along the axis of the rod, there is propagation of perturbations from the disk as observed in experiments. In simulations, the period of temperature perturbations is in good agreement with experimental results. An instability due to coupling of heat flux and the magnetic field advection provides a possible explanation for perturbation growth along the axis of the rod, and the instability growth rate is consistent with experimental results.

DOI: 10.1103/PhysRevE.109.015207

I. INTRODUCTION

Several approaches to inertial confinement fusion (ICF) use lasers coupled to magnetized plasmas. The most well-known approach is magnetized liner inertial fusion at Sandia National Laboratory (MagLIF) where the Z machine generates $\vec{j}\times\vec{B}$ (where $\vec{j}$ is the current density and $\vec{B}$ is the magnetic field) force to drive the implosion [1,2]. Currently, there are many platforms in development, three platforms that are based on cylindrical geometry: –MagLIF, –mini-MagLIF on OMEGA laser system at the Laboratory for Laser Energetics, and –magnetized hohlraums at Lawrence Livermore National Laboratory have incorporated external magnetic fields and implosions that are modified by thermal effects from lasers acting as either a driver or a heater or both [2–4]. The combination of megagauss magnetic fields and high-energy lasers enables access to an interesting parameter space where the magnetic pressure is comparable to the plasma thermal pressure with the parameter $\beta = p_{\text{therm}}/p_{\text{mag}} = nT/(B^2/8\pi)$ close to unity, where n is the total number density and T is the temperature. For effective confinement of alpha particles due to the magnetic field, the compressed magnetic field in an implosion would need to be strong enough that thermal pressure and magnetic pressure become comparable [5].

Experiments at the University Nevada, Reno have been investigating the parameter space where high-energy lasers are coupled with megagauss magnetic fields [6–8] exploring thermal and field transport in highly magnetized thermal plasma. Experiments observed the generation of plasma structures that were a consequence of the interplay between thermal and magnetic-field transport in a plasma. In the experiments we are modeling, the Leopard laser with a single beam at wavelength $\lambda = 1.06\,\mu$m, a laser pulse duration of 0.8 ns and intensity of 3×10^{15} W/cm^2, focused to a spot-size of 30 μm was used to ablate plasma from the surface of a current-carrying rod. The current was driven by the Zebra pulsed-power machine and reached up to 1 MA, with associated magnetic fields of $2-3$ MG measured at the rod surface. Shadowgrams taken in the direction perpendicular to the cylinder axis showed a collimated plasma jet on the front end where the laser was focused, as well as a corresponding jet on the other side of the rod (the back end). Two-dimensional simulations were able to describe the collimation and structure of the ablated plasma that transitions from $\beta > 1$ to $\beta \leqslant 1$ [9]. In the plasma, there are regions where the Hall parameter ($\chi = \omega_e\tau_{ei}$, where ω_e is the electron Larmor frequency and $\tau_{ei} = \lambda_e/v_{th}$ is the electron collision time, v_{th} is the thermal velocity, and λ_e is the electron mean-free path) was close to or slightly below unity. Modeling the plasma dynamics in the azimuthal direction is key to understanding the generation of plasma on the back end of the rod. Even with a strong magnetic field in the plasma, transport in the direction parallel to the field lines is usually treated similar to an unmagnetized plasma. When electron mean-free paths λ_e are

*leal9@llnl.gov

long in the laser-generated plasma, the local approximation for heat transport is no longer valid. As kinetic modeling is computationally expensive, more tractable three-dimensional hydrodynamic modeling is applied to provide an explanation of the plasma structure.

II. THEORY AND SIMULATION SETUP

The arbitrary Lagrangian Eulerian radiation-hydrodynamic code HYDRA with its MHD package has been used extensively to model MHD effects relevant to ICF [10,11]. HYDRA is a multiphysics code with the capability to include extended Ohm's law and anisotropic heat conduction for both electrons and ions with transport coefficients calculated from Braginskii formalism [12]. Ohm's law for the plasma corresponds to neglecting electron inertia in the electron momentum equation. After substituting the electric field from Ohm's law into Faraday's law, advection of the magnetic field is described by the following equation:

$$\frac{\partial \vec{B}}{\partial t} = -c\nabla \times \left[-\frac{1}{c}\vec{V} \times \vec{B} + \frac{1}{(cen_e)}\vec{j} \times \vec{B} - \frac{1}{en_e}\nabla \cdot \overleftrightarrow{p_e} + (\overleftrightarrow{\eta} \cdot \vec{j} - \overleftrightarrow{\beta} \cdot \nabla T_e) \right]. \quad (1)$$

Here $\overleftrightarrow{p_e}$ is the electron pressure tensor, $\vec{V}$ is the bulk plasma velocity, e is the electron charge, and c is the speed of light. $\overleftrightarrow{\eta}$ and $\overleftrightarrow{\beta}$ are Braginskii transport tensors, and any arbitrary tensor $\overleftrightarrow{\psi}$ acts on an arbitrary vector $\vec{s}$ in the following way: $\overleftrightarrow{\psi} \cdot \vec{s} = \psi_\parallel \hat{B}(\hat{B} \cdot \vec{s}) + \psi_\perp \hat{B} \times (\vec{s} \times \hat{B}) \pm \psi_\wedge \hat{B} \times \vec{s}$ (where $+$ is for $\overleftrightarrow{\beta}$, $\overleftrightarrow{\kappa}$, and $-$ is for $\overleftrightarrow{\eta}$). The elements of the transport tensors are calculated using ratios of polynomial fits that are functions of the Hall parameter χ. The polynomial fits are obtained from the linearization of the Fokker-Planck equation for the distribution function and calculating first-order correction to the distribution function [12]. The advection of field along the temperature gradient is governed by the Nernst effect associated with the $\beta_\wedge$ component [13,14]. The cross-gradient advection of magnetic fields (cross-gradient Nernst effect) is associated with the $(\beta_\parallel - \beta_\perp)$ component and can twist the magnetic field in the direction perpendicular to both the temperature gradient and the magnetic field.

The transport tensors define the electron heat flux:

$$\vec{q}_e = -\overleftrightarrow{\kappa} \cdot \nabla T_e - \overleftrightarrow{\beta_q} \cdot \vec{j}, \quad (2)$$

where the tensor $\overleftrightarrow{\beta_q} = T_e \overleftrightarrow{\beta}$. Here the tensor elements β_q are associated with the Ettinghausen effect, where coefficients of the elements are the same coefficients from the generalized Ohm's law—the square brackets of Eq. (1). We add the subscript just to denote when they are in the heat equation. The advection of strong magnetic fields can have a dramatic effect on heat conduction terms related to the presence of a magnetic field, such as the Righi-Leduc term. The Righi-Leduc term, which is associated with the coefficient $\kappa_\wedge$, drives the heat flux in the direction perpendicular to both the temperature gradient and field direction. In the experiments, magnetic-field advection can cause the initial azimuthal magnetic field to generate other field components. Another mechanism for the self-generation of magnetic fields is the Biermann battery effect [caused by the term $\nabla \overleftrightarrow{p_e}/en_e$ from Eq. (1)] that can also drive radial or axial magnetic fields. Modeling the interplay between the magnetic field and heat flux depends on the form of the transport coefficients.

Some transport coefficients initially obtained by Braginskii had inaccuracies of up to 65%. Corrected coefficients were calculated by Epperlein and Haines [15], and these coefficients represented the standard used in numerical codes for many years. Further calculations of the transport coefficients reduced the deviations for fits of transport coefficients to less than 1% of convergent of solutions as a function of Z, where a geometric method allowed the separation of equations for closure and equations where closure was used [16]. Recently, two groups found that further corrections to transport coefficients were needed to accurately model the magnetic field advection due to the cross-gradient Nernst effect [17,18]. One can write the transport coefficients as

$$\delta_\perp = \frac{\alpha_\wedge}{\chi}, \quad \gamma_\perp = \frac{\beta_\wedge}{\chi}, \quad (3)$$

$$\delta_\wedge = \frac{\alpha_\perp - \alpha_\parallel}{\chi}, \quad \gamma_\wedge = \frac{\beta_\perp - \beta_\parallel}{\chi}, \quad (4)$$

where $\alpha_a = \frac{\eta_a}{en_e}$, $a = \perp - \parallel$, and $\wedge$. The new Davies-Wen [18] and Sadler-Walsh [17] coefficients were shown to be in good agreement with each other [19], where the Sadler-Waslh coefficients used the usual Chapman-Enskog method and the Davies-Wen coefficients are formulated in the same method as Ji and Held. The complete model of plasma evolution also includes the continuity and momentum equations. In plasmas where the plasma parameter β is close to unity, variation in heat flux and magnetic-field advection can change the behavior of the bulk plasma motion via the momentum equation. If the magnetic pressure is acting against the thermal pressure, any decrease in field strength or increase in thermal pressure would influence the plasma expansion. Three-dimensional HYDRA simulations were carried out in cylindrical geometry with 100 axial zones, 150 radial zones, and 180 azimuthal zones. Of the 150 radial zones, 20 radial zones in the vacuum region of hydrogen where the density is set to the density floor of 1×10^{17} cm^{-3}, 50 radial zones are placed in the 20-micron-thick region of the Al rod surface, then the final 40 zones that increase in size toward the center so 40 axial zones begin within the laser spot size. The rod diameter is 1 mm, and in simulations the axial size is taken at 2 mm. The axial zones are centered at the laser spot so 30 zones are within the laser spot. The azimuthal zones are spaced equally around the rod. An azimuthal magnetic field is imposed on the boundary of the simulation domain such that an axial current is generated on the rod surface and azimuthal field at the surface is 3 MG. The radial simulation domain extends to 8 mm. After the magnetic field is imposed, a density gradient is generated by the driven current at the surface of the rod. After the magnetic field at the surface is stable, laser ablation is modeled using laser ray-trace deposition with a pulse of 0.8 ns—same as experiments. All terms in Ohm's law are included except for the Hall term $\frac{1}{en_e}\vec{j} \times \vec{B}$ [from Eq. (1)], which at the time of producing these simulations was not numerically stable. As such, this study is focused on the effects of extended-MHD effects of heat flux and Nernst effect in

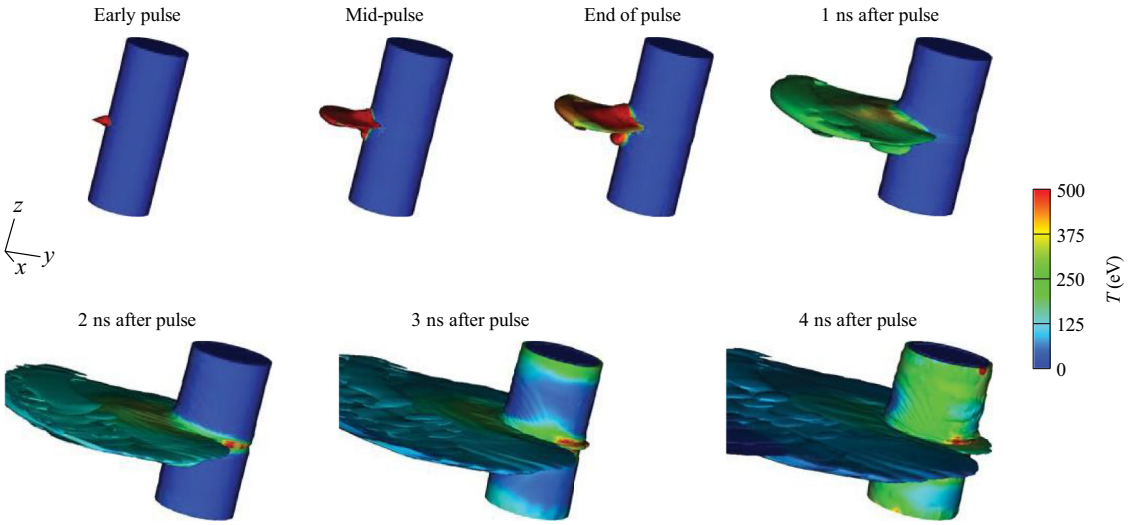

FIG. 1. Isovolume plot of electron temperature at different times showing formation of disk plasma.

generating the localized plasma structure. In neglecting the Hall term, the low-density Al plasma produced by the axial current and its interaction with the vacuum region before laser ablation is not fully captured [20].

III. RESULTS OF HYDRA SIMULATIONS

In simulations, the laser generated a hot spot on the surface of the rod. Heat flux is limited in the axial direction by the azimuthal magnetic field. The heat flow in the azimuthal direction is unaffected by the field. The asymmetry in heat conduction generates temperature gradients in the radial direction localized axially. The temperature gradient can advect magnetic field radially (depending on the transport coefficients used, which will be discussed in detail in the following sections). This process leads to thermal pressure in the plasma being strong enough to drive plasma radially outward from the rod.

The magnetic field generates magnetic pressure against the expanding plasma and leads to a pinching effect where the field flattens the ablation plasma. This effect produces a plasma feature that is axially confined by the magnetic field, where the shape is dependent on the field lines that surround it.

Figure 1 shows the evolution of the plasma disk using the isovolume plot of electron temperature. Similarly to the two-dimensional simulations, the plasma undergoes a pinching phase (from the midpulse to end-of-pulse phase in Fig. 1) when the azimuthal magnetic fields pinch the ablated plasma [9]. In three-dimensional simulations, the ablated plasma flows around the rod from the laser side (from 1 ns after the pulse to 4 ns after the pulse in Fig. 1) but does not fully expand to surround the rod at times up to 14 ns, which is the time range captured by experimental diagnostics. The plasma at the back end of the rod is not the result of the expansion of plasma from the front end, but rather comes from the ejecta at the back end.

Results of the simulations shown in Fig. 1 used updated transport coefficients from Ref. [17]. Figure 2 illustrates how the shape of the plasma in simulations depends on different transport coefficients. In simulations using Braginskii coefficients, the heat flux around the rod is essentially damped and the structures at the back end of the rod do not exist. Heat flux is dominated by terms with $\beta_{\wedge,q}$ and $\kappa_{\wedge}$, which are known to have inaccuracies in the Braginskii model. In simulations with the more recent transport coefficients (Epperlein-Haines and Sadler-Walsh), the heat flux from the laser spot side propagates along the surface of the rod in the azimuthal direction. The heat flux from the hot spot generates enough thermal

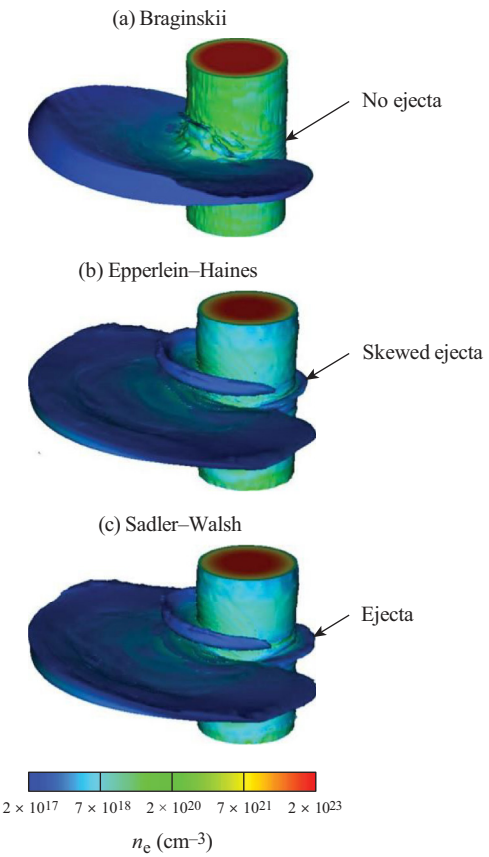

FIG. 2. Isovolume plot of electron density at 6 ns after the laser pulse in simulations using three different sets of coefficients

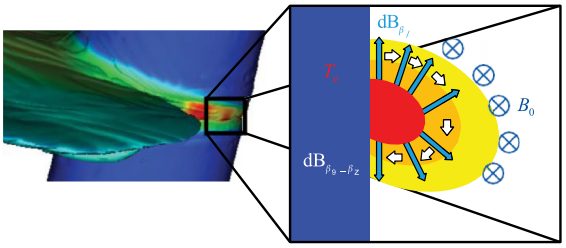

FIG. 3. Schematic of magnetic-field advection by Nernst effect $\beta_\wedge$ (blue arrows) and cross-gradient Nernst effect $\beta_\parallel - \beta_\perp$ (white arrows).

pressure to push plasma out radially along the surface of the rod, forming the back-end ejecta.

The choice of transport coefficients can determine the curvature of the back-end ejecta. Figure 3 shows a schematic of field advection in a skewed temperature gradient. In the magnetic field B_0 perpendicular to the plane of Fig. 3, the Nernst effect is illustrated by blue arrows and the cross-gradient Nernst effect is illustrated by white arrows. The Nernst effect advects the magnetic field to the edge of the plasma and the cross-gradient Nernst effect twists the magnetic field in a skewed temperature gradient. The curvature of the magnetic field plays an important role in shaping the expanding plasma, including the back-end ejecta. In Fig. 4, a comparison of density plots from simulations with Sadler-Walsh coefficients and Epperlein-Haines coefficients shows that the Sadler-Walsh corrections to cross-gradient terms change the direction of the field advection due to heat flux from the laser spot. In the case of Epperlein-Haines coefficients, the back-end ejecta is skewed, thus limiting the radial expansion. In the case of Sadler-Walsh transport coefficients, the back-end ejecta is captured more accurately and a more complete disk is formed. Heat flux from the laser spot drives the formation of a disk, and axial magnetic fields generated by Biermann battery may restrict heat flux and change the direction of the Righi-Leduc heat flux. Recent studies have shown possible suppression of Biermann battery fields and of the Nernst effect [21], which was attributed to the nonlocality of the heat flux characterized by the ratio of electron mean-free path λ_e to the temperature-scale length l_t [22]. For the simulations presented here, the Biermann generated fields are mostly in the region

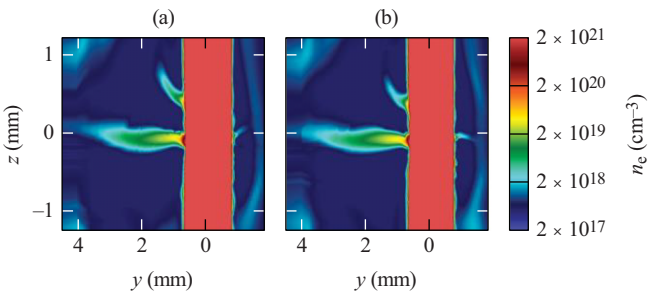

FIG. 4. Two-dimensional cross section of electron density at 6 ns after the laser pulse in simulations using (a) Epperlein-Haines and (b) Sadler-Walsh coefficients. The ejecta in the back-end structure is straighter and extends farther in simulations using Sadler-Walsh coefficients.

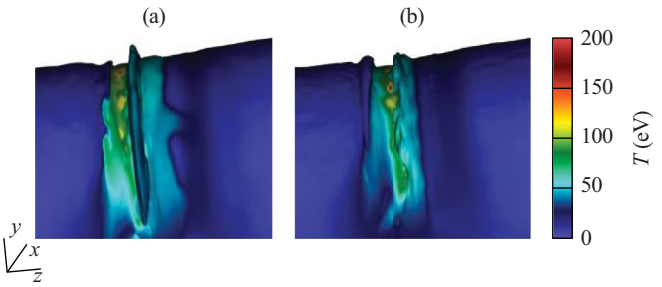

FIG. 5. Electron temperature near the disk back end at 3 ns after the laser pulse in simulation with classical Nernst coefficient (a) and Nernst coefficient reduced to 0.2 of classical value (b). In the simulations with reduced Nernst coefficient, the back-end cavitation is observed instead of the back-end ejecta in (a).

where heat flux is local. To evaluate the importance of the Nernst effect, a simulation with the Nernst coefficent reduced to 0.2 of its classical value was performed. The comparison of simulation results with the classical Nernst coefficient and reduced Nernst coefficient is shown in Fig. 5. Figure 5 shows that with reduced Nernst coefficient, the generation of the back-end ejecta is suppressed and a cavity occurs instead.

A. Comparing synthetic shadowgrams to experiments

In experiments, the plasma was imaged using shadowgrams for laser-probing wavelengths of 532 nm and 266 nm for 0.2 ns exposure times. To compare simulations to experiments, synthetic shadowgrams from HYDRA simulations were generated. A ray-trace algorithm was developed in Python to postprocess HYDRA simulations and to generate simulated shadowgrams (Appendix). The density gradients are calculated in simulations and the rays are propagated through the simulation volume. The rays either are deflected by the density gradient and collisionally absorbed or transmit through the plasma and are recorded on a 500 x 500 pixel plane.

In Fig. 6, the synthetic shadowgrams from simulations using different transport coefficients are compared to experimental shadowgrams. The plasma collimation on the laser side in synthetic shadowgrams matches the general structure seen in experiments. In simulations using Sadler-Walsh coefficients, the formed back-end ejecta is less skewed and expands further radially compared to the simulation using Epperlein-Haines coefficients. Experimental shadowgrams using probing lasers wavelengths of 532 nm and 266 nm both clearly show the back-end plasma. In simulations, the back-end structure is smaller. The disk is more clearly seen in both 532 nm and 266 nm shadowgrams from simulations using Sadler-Walsh coefficients compared to simulations using Epperlein-Haines coefficients. Still, simulations have a smaller ejecta compared to experiments and a less dense structure. Simulations have smaller width and size of the disk than in experiments. The synthetic shadowgrams are produced from snapshots in time and do not fully account for dynamic plasma evolution, which may explain some of the discrepancies between simulations and experiments. However, the exposure time is at 0.2 ns, so while this may affect some cosmetic features, while not exact we should be qualitatively

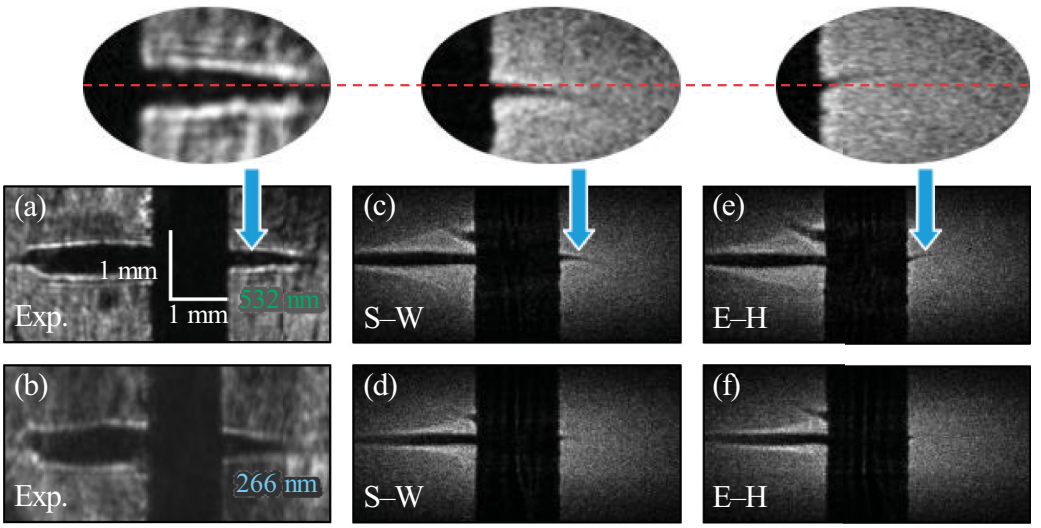

FIG. 6. Shadowgrams at 6 ns after the laser pulse for probing laser wavelengths of 532 and 266 nm from experiments [(a) and (b), respectively] from simulations using Sadler-Walsh coefficients [(c) and (d), respectively] and using Epperlein-Haines coefficients [(e) and (f), respectively].

similar. Another possible source of discrepancies is that the initial conditions of the low-density plasma surrounding the wire before the laser pulse starts are difficult to accurately capture in hydrocodes and are not fully characterized in experiments.

B. Kinetic considerations

In our simulations, we are neglecting nonlocal effects. A measure of kinetic effects can be the ratio of the ion mean-free path and ion temperature scale length λ_i/L_{T_i}, which is below 0.01 in most of the Al plasma coming from the rod after the driving pulse as shown in Figs. 7(a) and 7(b). However, this ratio does grow in low-density edges as the plasma drops closer to the hydro vacuum density. The vacuum has been a known issue for hydro simulations and is outside the scope of this paper [20]. It should also be noted that in directions perpendicular to the magnetic field, the ion Larmor radius can be significantly smaller than the mean-free path that would mediate transport. In Figs. 7(c) and 7(d), the ratio of ion Larmor radius r_i to temperature scale length has values much lower than 0.01. We focus our study on the denser plasma ablating off the rod surface and pushing against the magnetic field that is initialized to be like that seen in experiments. During the laser pulse, the ion kinetic effects may be important and a kinetic modeling study may be required. The

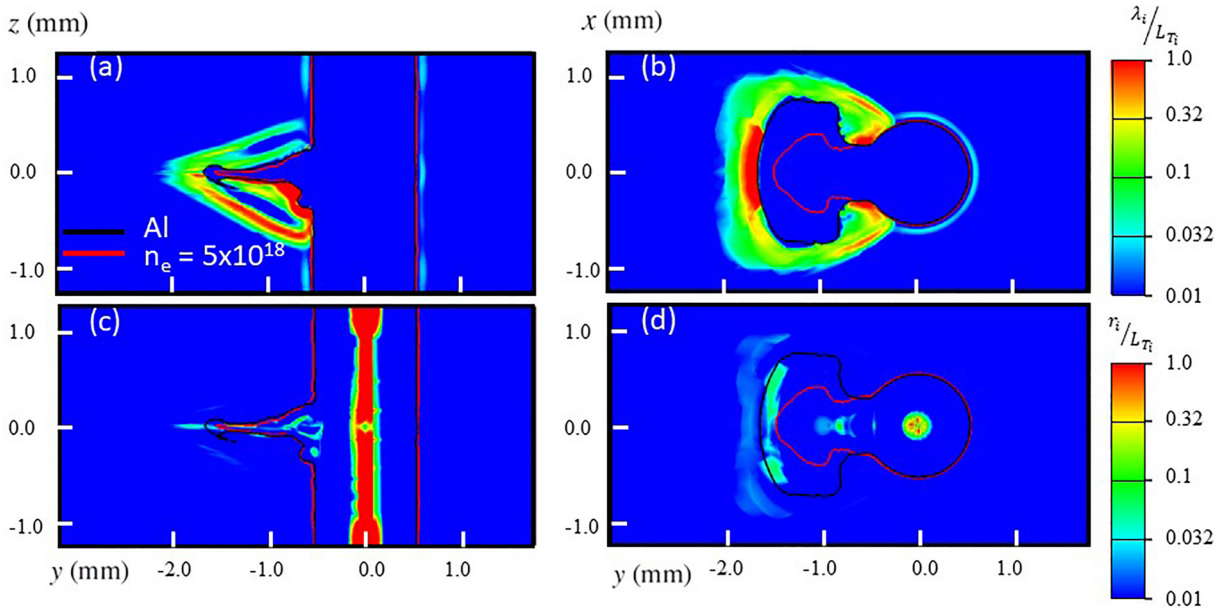

FIG. 7. Two-dimensional cross sections immediately after the laser pulse ends for the ratio of ion mean-free path to ion temperature scale length at $x = 0$ (a) and $z = 0$ (b) and for the ratio of ion Larmor radius to ion temperature scale length at $x = 0$ (c) and $z = 0$ (d). The red (light) contour denotes electron densities above $5 \times 10^{18}\text{cm}^{-3}$ and the black (dark) contour denotes Al plasma.

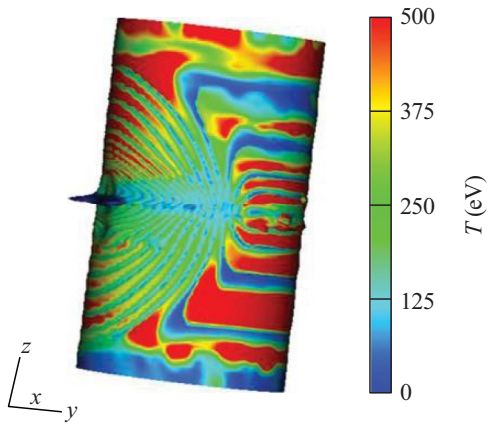

FIG. 8. Isovolume plot of electron temperature at electron densities larger than critical density n_c at 6 ns after the laser pulse. In the axial direction, temperature perturbations expand away from the laser spot.

disk is formed at times about four times greater that the pulse length. There may be an influence of kinetic effects during and immediately after the laser pulse but it is unlikely to change the qualitative picture of disk formation.

IV. INSTABILITY IN AXIAL DIRECTION

A feature seen in experimental shadowgrams and in simulations is the formation of perturbations in the axial direction on the surface of the rod. In simulations, these temperature perturbations are generated during the laser pulse. Figure 8 shows an isovolume plot of electron temperature, with perturbations forming during laser ablation, where we plot the volume above the critical density n_c. The critical density for a given laser wavelength is the density beyond which light

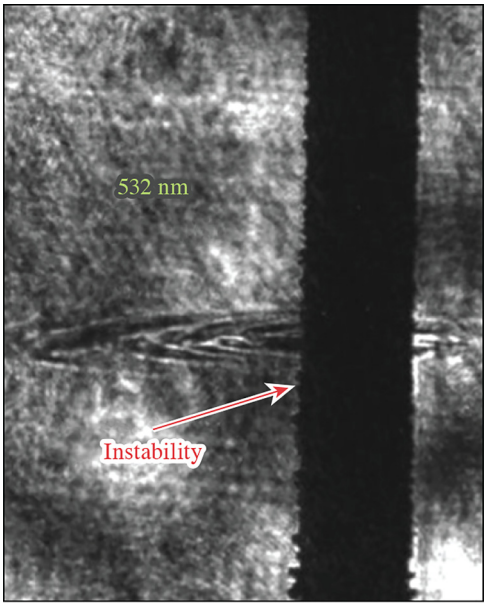

FIG. 9. Shadowgram from experiments with probing laser wavelength of 532 nm at 14 ns after the laser pulse showing perturbations along the rod.

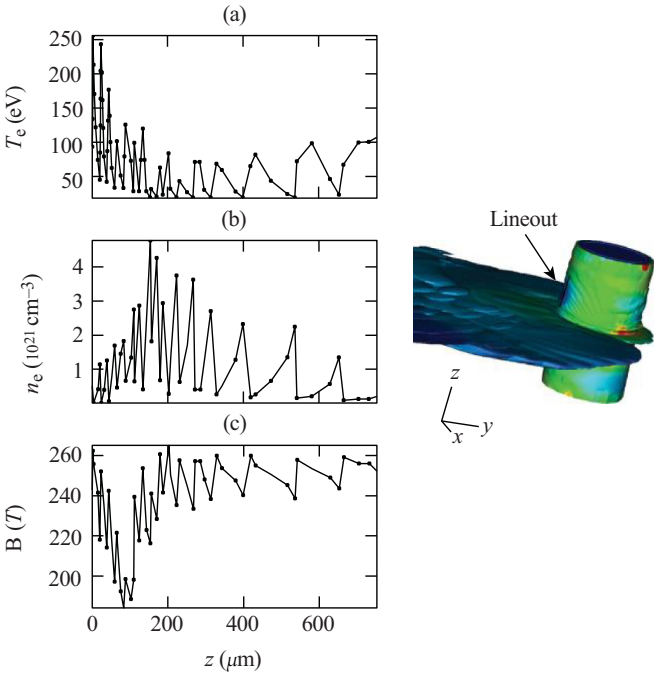

FIG. 10. Line outs of electron density, temperature, and magnetic field in the axial direction along the rod surface starting from the axial bottom of the disk at 4 ns after laser pulse. The period of perturbations is smaller closer to the disk.

cannot propagate (for a wavelength of 1.06 μm, this is at 1.1×10^{21} cm^{-3}). These perturbations expand away from the laser spot and have a smaller period closer to the disk. For comparison, Fig. 9 shows perturbations along the surface of the rod in experiments at 14 ns after the end of the laser pulse. The angle at which the shadowgram is taken is slightly tilted for a better view. Figure 10 shows axial line outs of electron density, temperature, and magnetic field along the rod surface, starting at the bottom edge of the disk and extending down. The wavelength of these perturbations is close to 20 μm near the disk and increases away from the disk. We can treat these perturbations as generated near the disk region, and use linear theory to describe their formation. We focus on the temperature perturbations and note that any perturbation in temperature would lead to density perturbations on the rod surface. To describe these perturbations, a model for field-compressing magnetothermal instability is suggested. The model uses two coupled equations: heat flux equation and Faraday's law, with the electric field given by Ohm's law collisional terms:

$$\frac{3}{2} n_e \frac{\partial T}{\partial t} = -\nabla \cdot (-\overleftrightarrow{\kappa} \cdot \nabla T - \overleftrightarrow{\beta} \cdot (\nabla \times \vec{B})), \quad (5)$$

$$\frac{\partial \vec{B}}{\partial t} = -\nabla \times (\overleftrightarrow{\eta} \cdot (\nabla \times \vec{B}) - \overleftrightarrow{\beta} \cdot \nabla T). \quad (6)$$

A similar instability was described earlier in the case of an axial magnetic field [23]. The dominant terms driving the instability in Ref. [23] were the Nernst and Righi-Leduc terms.

Further studies have focused on the magnetothermal instability from laser-generated magnetic fields in a uniform medium [24,25]. Recent work focused on a nonuniform

medium to study whether the instability growth is convective or absolute [26].

Here we show that instability growth driven by the terms with $\beta_\wedge$ coefficients, i.e., the Nernst term in Eq. (5) and the Ettingshausen term in Eq. (6), is a possible candidate to explain experimental results when using Davies-Wen coefficients for β and η and Ji-Held transport coefficients for κ [16,18] and maintaining derivatives of all transport coefficients. We refer to it as current-driven magnetothermal instability since the Ettingshausen term depends on the current. We consider wavelike perturbations in temperature and magnetic field,

$$T = T_0(r,z,t) + T_1 \exp i(k_z z + k_r r - \omega t), \tag{7}$$

$$B = (B_0(r,z,t) + B_{1\theta} \exp i(k_z z + k_r r - \omega t))\hat{\theta}, \tag{8}$$

where T_0 and B_0 are the unperturbed values and T_1 and B_1 are wavelike perturbations with wave vectors in axial and radial directions k_z and k_r and frequency ω. In our case, the magnetic-field perturbations are considered only in the azimuthal direction $\hat{\theta}$. After substituting Eqs. (7) and (8) into (5) and (6), the dispersion relation can be obtained using linear perturbation theory, and the instability growth rate is the positive imaginary part of frequency in the dispersion relation. The dispersion relation can be written in terms of various transport coefficients

$$C_l = \chi\left(\frac{1}{l_b} + \frac{3}{2l_t}\right) \tag{9}$$

$$C_\kappa = -\frac{2}{3n_e}\left[-\kappa_\perp\left(-\frac{ik_r}{r} + k_r^2 + k_z^2\right) + \kappa_\wedge \frac{ik_z}{r} + C_l\left(\frac{\partial \kappa_\perp}{\partial \chi}(ik_r + ik_z) + \frac{\partial \kappa_\wedge}{\partial \chi}(ik_z - ik_r)\right)\right], \tag{10}$$

$$C_{\beta,q} = \frac{2}{3n_e}\left[-\beta_{\wedge,q}\left(k_r^2 + k_z^2 - 2\frac{ik_r}{r}\right) + C_l\left(\frac{\partial \beta_{\wedge,q}}{\partial \chi}\left(\frac{1}{r} + ik_r + ik_z\right) - \frac{\partial \beta_{\perp,q}}{\partial \chi}\left(ik_z - ik_r - \frac{1}{r}\right)\right)\right], \tag{11}$$

$$C_{\beta,b} = -\left[\beta_\wedge k_z^2 + \beta_\wedge k_r^2 - C_l\left(\frac{\partial \beta_\perp}{\partial \chi}(ik_r - ik_z) + \frac{\partial \beta_\wedge}{\partial \chi}(ik_z + ik_r)\right)\right], \tag{12}$$

$$C_\eta = \left[\frac{\eta_\perp}{r^2} + \eta_\perp k_z^2 - \eta_\wedge \frac{ik_z}{r} - \eta_\perp \frac{ik_r}{r} - \eta_\perp k_r^2 - C_l\left(\frac{\partial \eta_\perp}{\partial \chi}\left(ik_r + ik_z + \frac{1}{r}\right) + \frac{\partial \eta_\wedge}{\partial \chi}\left(ik_r + \frac{1}{r} - ik_z\right)\right)\right], \tag{13}$$

where each relation is dependent on the transport coefficients from anisotropic heat conduction κ, the electrothermal terms with β_q from the heat equation, the diffusive terms with η, and the electrothermal terms with β from Ohm's law. The subscripts q and b correspond to coefficients originating from the heat equation Eq. (2) (q) and the field advection equation Eq. (1) (b). Here l_b and l_t are the scale lengths for the magnetic field and electron temperature. The dispersion relation can then be written as

$$0 = C_\eta C_\kappa - C_{\beta,b}C_{\beta,q} - i(C_\eta + C_\kappa)\omega - \omega^2. \tag{14}$$

Using the transport coefficients from Refs. [16,18], the instability growth rate is obtained by solving Eq. (12). When solving Eq. (12), terms with $1/r$ are negligible since the radius curvature is much larger than the scale lengths of importance. We can solve Eq. (14) using three sets of transport coefficients Epperlein-Haines [15], Sadler-Walsh [17], and Davies-Wen [18]. Even though Davies-Wen coefficients, as mentioned earlier, have been found to be in good agreement with Saddler-Walsh coefficients [19], we see a difference in the growth rates for the instability. In Fig. 11, the solutions that have positive imaginary parts are plotted for all coefficients. In all cases, instability growth is possible. The growth rates for the instability are increased by about a factor of 2 in the solutions using the Davies-Wen coefficients compared to Epperlein-Haines coefficients, and a factor of 4 when compared to the Sadler-Walsh coefficients. This implies that the functional form of the transport coefficients is of great importance for the transport coefficients in calculating the growth rate. The spatial scales for the $k_z > 0.5$ (1/μm) and timescales of instability growth at $1-2$ ns agree with the experimental results. In Fig. 12, we show the growth rate for different density values over electron temperature. At quarter critical density, the growth rate peak is at 120 eV with a value of 1.2 GHz. For densities near critical density, the peak is at 230 eV and the growth rate is 0.78 GHz.

V. CONCLUSIONS

In this paper, we have examined the major aspects of the plasma disk formation that can be modeled by extended magnetohydrodynamics including three-dimensional effects. The simulations reproduce the collimated ablation plasma on the laser side of the rod as well as the back-end ejecta. The shape of the plasma formed is dependent on magnetic-field curvature. The back-end ejecta is not the product of simple hydrodynamic expansion around the rod but is generated via heat transport around the rod. Simulations using Braginskii transport coefficients do not fully model heat flux from the laser spot around the surface of the rod and do not produce the back-end ejecta. Simulations using Epperlein-Haines transport coefficients lead to skewing of the plasma ejecta at the back end. Simulations using the recent Sadler-Walsh transport coefficients show the best agreement with experiments because the cross-gradient Nernst advection of the magnetic fields is not exaggerated and, consequently, the ejecta direction is not skewed by the magnetic fields. Artificially lowering Nernst coefficients leads to the damping of the ejecta expansion. The structure of the plasma is largely described by our simulations, but kinetic effects and the inclusion of the Hall term could further improve agreement between simulations and experiments. In simulations, perturbations propagate in the axial direction on the surface of the rod, as seen in experiments. A possible instability in the axial direction is described with growth rates consistent with timescales of

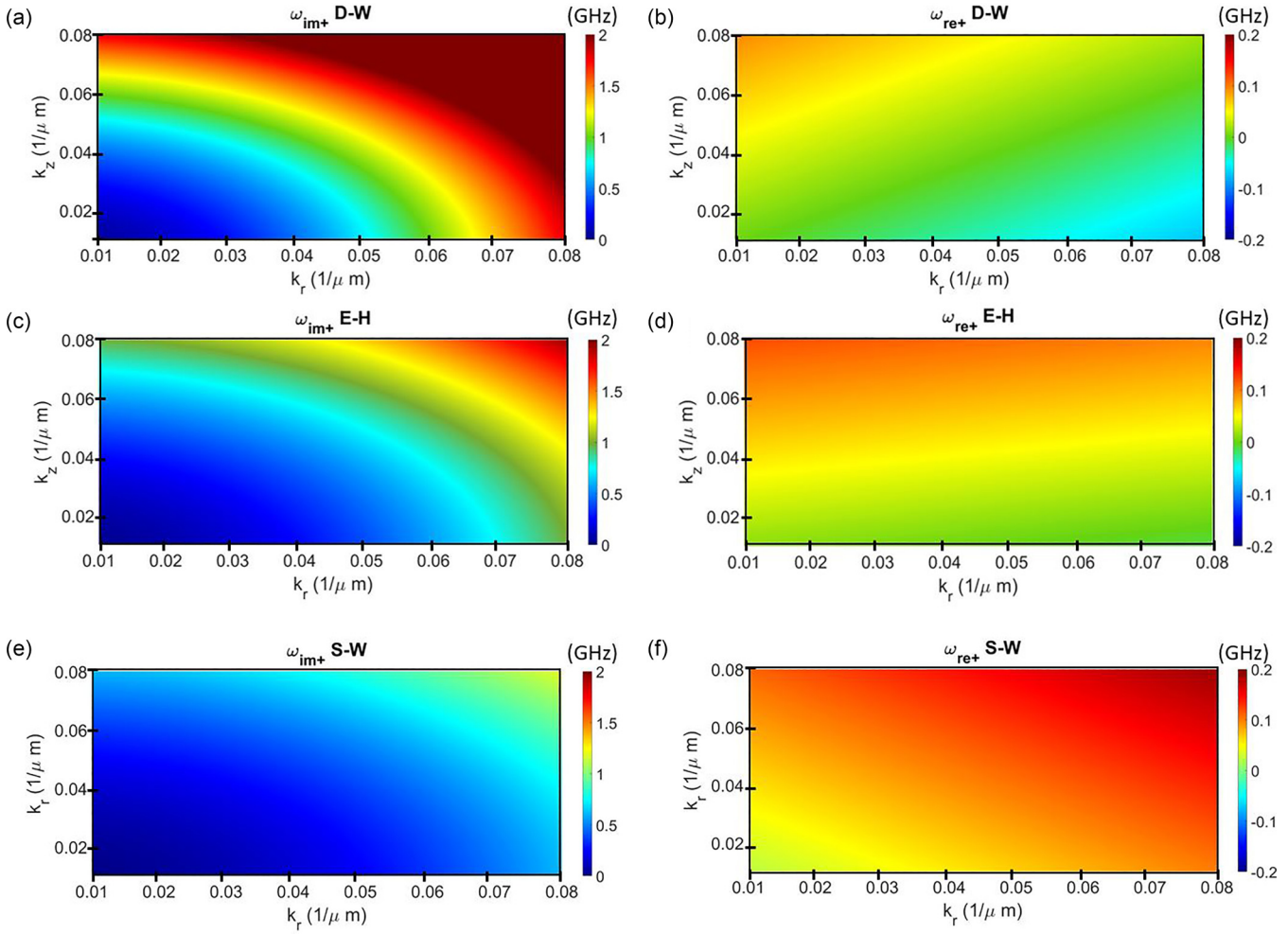

FIG. 11. Solutions for real and imaginary parts of frequency ω (GHz) using Davies-Wen coefficients (a) and (b), Epperlein-Haines coefficients (c) and (d), and Sadler-Walsh coefficients (e) and (f). The parameters used are $T_e = 150$ eV, $n_e = n_c = 1.1 \times 10^{21}\text{cm}^{-3}$, $B = 200\,T$, and $l_b = l_t = 100\,\mu\text{m}$.

experiments. This current-driven magnetothermal instability may be important for cylindrical plasmas where temperature perturbations can be generated via another coupling mechanism. The functional form of the coefficients vary between their different calculations. The coefficients calculated by Davies-Wen give the fastest growth rate compared to Sadler-Walsh or Epperlein-Haines coefficients.

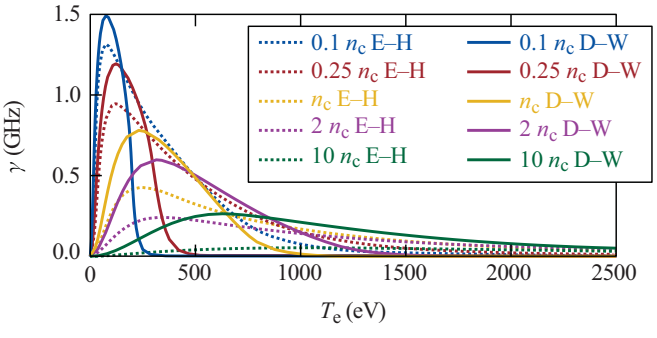

FIG. 12. The growth rate as a function of electron temperature at various electron densities calculated with either Epperlein-Haines or Davies-Wen Coefficients. Parameters: $k_r = .05$ (1/μm), $k_r = 0.01$ (1/μm), $l_b = l_t = 100$, μm, and $B = 200\,T$.

ACKNOWLEDGMENTS

We acknowledge the support of LLNL computational resources and the working group of HYDRA lead by Dr. Marinak. This material is based upon work supported by the National Science Foundation Award No. PHY-1903355 and the Department of Energy National Nuclear Security Administration under Award No. DE-NA0003856, the University of Rochester, and the New York State Energy Research and Development Authority. This work was performed under the auspices of the U.S. Department of Energy by Lawrence Livermore National Laboratory under Contract No. DE-AC52-07NA27344. This document was prepared as an account of work sponsored by an agency of the U.S. Government. Neither the U.S. Government nor Lawrence Livermore National Security, LLC, nor any of their employees makes any warranty, expressed or implied, or assumes any legal liability or responsibility for the accuracy, completeness, or usefulness of any information, apparatus, product, or process disclosed,

APPENDIX: SHADOWGRAPHY METHODOLOGY

The synthetic shadowgraphy routine is a Python postprocessing code used to generated synthetic shadowgrams from three-dimensional simulations. HYDRA simulation output is regridded onto Cartesian space with grid size 500 x 500 x 500. A plasma object is generated with attributes for electron density, electron temperature, ion temperature, electron density gradients in each direction, and atomic number. Rays are also treated as objects with attributes for $\vec{k}$, velocity $\vec{v}$, and intensity normalized. Using the relation for the refractive index,

$$n^2 = 1 - \frac{n_e}{n_c}, \tag{A1}$$

the group velocity for each ray can be approximated as

$$\frac{\partial \vec{v}_g}{\partial t} = -\frac{c^2}{2}\frac{\nabla n_e}{n_c}. \tag{A2}$$

As the rays pass through the gradient of the plasma, they are deflected from their initial trajectory chosen by the user. The code updates iteratively with $dt = (x_{\max})C_{cfl}/c$, where $x_{\max}$ is the grid size and C_{cfl} is a courant number.After a ray is deflected outside the simulation grid, the ray is ended and not tracked through the system. Rays are also treated as collisionally absorbed via the calculated fraction of absorption [27],

$$f_a = 1 - \exp\left(-\int_{-\infty}^{0} 2im(k(x))dx\right), \tag{A3}$$

where we take the imaginary part of the solution to the dispersion relation k [28]. The fraction of the laser energy still in the ray f_l is

$$f_l = \exp\left(-\int_{-\infty}^{0} 2im(k(x))dx\right). \tag{A4}$$

Considering infinitesimal moments of time and taking the group velocity as $v_g = dx/dt$, we have the fraction of the laser not absorbed at time dt,

$$df_l = \exp(-2im(k)v_g dt), \tag{A5}$$

$$df_l = \exp\left(-2\frac{\upsilon_{ce}n_e^2}{cn_c^2}dt\right), \tag{A6}$$

where we have substituted the dispersion relation $\mathrm{Im}(k)$ as

$$\mathrm{Im}(k) = \frac{\upsilon_{ce}}{c}\frac{n_e^2/n_c^2}{\sqrt{1 - n_e/n_c}} \tag{A7}$$

υ_{ce} is the collision frequency of electrons at the critical density. The script makes use of the multiprocessing tool in Python so each core of an associated node tracks one ray and immediately starts another ray independently of what the other cores are doing.

[1] Stefano Atzeni and Jürgen Meyer-ter Vehn, *The Physics of Inertial Fusion: Beam Plasma Interaction, Hydrodynamics, Hot Dense Matter* (Oxford University Press, Oxford, 2004), Vol. 125.

[2] A. B. Sefkow, S. A. Slutz, J. M. Koning, M. M. Marinak, K. J. Peterson, D. B. Sinars, and R. A. Vesey, Design of magnetized liner inertial fusion experiments using the Z facility, Phys. Plasmas **21**, 072711 (2014).

[3] J. R. Davies, D. H. Barnak, R. Betti, E. M. Campbell, P.-Y. Chang, A. B. Sefkow, K. J. Peterson, D. B. Sinars, and M. R. Weis, Laser-driven magnetized liner inertial fusion, Phys. Plasmas **24**, 062701 (2017).

[4] J. D. Moody, B. B. Pollock, H. Sio, D. J. Strozzi, D. D.-M. Ho, C. Walsh, G. E. Kemp, S. O. Kucheyev, B. Kozioziemski, E. G. Carroll *et al.*, The magnetized indirect drive project on the national ignition facility, J. Fusion Energy **41**, 7 (2022).

[5] L. J. Perkins, D. D.-M. Ho, B. G. Logan, G. B. Zimmerman, M. A. Rhodes, D. J. Strozzi, D. T. Blackfield, and S. A. Hawkins, The potential of imposed magnetic fields for enhancing ignition probability and fusion energy yield in indirect-drive inertial confinement fusion, Phys. Plasmas **24**, 062708 (2017).

[6] V. V. Ivanov, A. V. Maximov, R. Betti, P. P. Wiewior, P. Hakel, and M. E. Sherrill, Generation of disc-like plasma from laser-matter interaction in the presence of a strong external magnetic field, Plasma Phys. Control. Fusion **59**, 085008 (2017).

[7] V. V. Ivanov, A. V. Maximov, R. Betti, L. S. Leal, R. C. Mancini, K. J. Swanson, I. E. Golovkin, Christopher John Fontes, H. Sawada, A. B. Sefkow *et al.*, Study of laser produced plasma in a longitudinal magnetic field, Phys. Plasmas **26**, 062707 (2019).

[8] V. V. Ivanov, A. V. Maximov, R. Betti, L. S. Leal, J. D. Moody, K. J. Swanson, and N. A. Huerta, Generation of strong magnetic fields for magnetized plasma experiments at the 1-MA pulsed power machine, Matter Radiat. Extremes **6**, 046901 (2021).

[9] L. S. Leal, A. V. Maximov, R. Betti, A. B. Sefkow, and V. V. Ivanov, Modeling magnetic confinement of laser-generated plasma in cylindrical geometry leading to disk-shaped structures, Phys. Plasmas **27**, 022116 (2020).

[10] M. M. Marinak, G. D. Kerbel, N. A. Gentile, O. Jones, D. Munro, S. Pollaine, T. R. Dittrich, and S. W. Haan, Three-dimensional hydra simulations of national ignition facility targets, Phys. Plasmas **8**, 2275 (2001).

[11] J. M. Koning, G. D. Kerbel, and M. M. Marinak, The hydra magnetohydrodynamics package, Bull. Am. Phys. Soc. **54**, NP8.10 (2009).

[12] S. I. Braginskii, Transport processes in a plasma, Rev. Plasma Phys. **1**, 205 (1965).

[13] C. A. Walsh, J. P. Chittenden, D. W. Hill, and C. Ridgers, Extended-magnetohydrodynamics in under-dense plasmas, Phys. Plasmas **27**, 022103 (2020).

[14] J. R. Davies, R. Betti, P.-Y. Chang, and G. Fiksel, The importance of electrothermal terms in Ohm's law for magnetized spherical implosions, Phys. Plasmas **22**, 112703 (2015).
[15] E. M. Epperlein and M. G. Haines, Phys. Fluids **29**, 1029 (1986).
[16] J.-Y. Ji and E. D. Held, Closure and transport theory for high-collisionality electron-ion plasmas, Phys. Plasmas **20**, 042114 (2013).
[17] J. D. Sadler, C. A. Walsh, and H. Li, Symmetric set of transport coefficients for collisional magnetized plasma, Phys. Rev. Lett. **126**, 075001 (2021).
[18] J. R. Davies, H. Wen, J.-Y. Ji, and E. D. Held, Transport coefficients for magnetic-field evolution in inviscid magneto-hydrodynamics, Phys. Plasmas **28**, 012305 (2021).
[19] C. A. Walsh, J. D. Sadler, and J. R. Davies, Updated magnetized transport coefficients: Impact on laser-plasmas with self-generated or applied magnetic fields, Nucl. Fusion **61**, 116025 (2021).
[20] C. E. Seyler, M. R. Martin, and N. D. Hamlin, Helical instability in MagLIF due to axial flux compression by low-density plasma, Phys. Plasmas **25**, 062711 (2018).
[21] P. T. Campbell, C. A. Walsh, B. K. Russell, J. P. Chittenden, A. Crilly, G. Fiksel, L. Gao, I. V. Igumenshchev, P. M. Nilson, A. G. R. Thomas *et al.*, Measuring magnetic flux suppression in high-power laser–plasma interactions, Phys. Plasmas **29**, 012701 (2022).
[22] M. Sherlock and J. J. Bissell, Suppression of the Biermann battery and stabilization of the thermomagnetic instability in laser fusion conditions, Phys. Rev. Lett. **124**, 055001 (2020).
[23] J. J. Bissell, C. P. Ridgers, and R. J. Kingham, Field compressing magnetothermal instability in laser plasmas, Phys. Rev. Lett. **105**, 175001 (2010).
[24] D. A. Tidman and R. A. Shanny, Field-generating thermal instability in laser-heated plasmas, Phys. Fluids **17**, 1207 (1974).
[25] L. A. Bol'shov and Dreĭ, Spontaneous magnetization of electronic thermal conductivity in a laser plasma.
[26] F. García-Rubio, R. Betti, J. Sanz, and H. Aluie, Theory of the magnetothermal instability in coronal plasma flows, Phys. Plasmas **29**, 092106 (2022).
[27] William Kruer, *The Physics of Laser Plasma Interactions* (CRC Press, New York, 2019).
[28] T. W. Johnson and J. M. Dawson, Correct values for high-frequency power absorption by inverse bremsstrahlung in plasma, Phys. Fluids **16**, 722 (1973).